



**HAL**  
open science

# Enhanced Stability and Bangap Tuning of $\alpha$ -[HC(NH<sub>2</sub>)<sub>2</sub>]PbI<sub>3</sub> Hybrid Perovskite by Large Cation Integration

Antonin Leblanc, Nicolas Mercier, Magali Allain, Jens Dittmer, Thierry Pauporté, Vincent Fernandez, Florent Boucher, Mikael Kepenekian, Claudine Katan

► **To cite this version:**

Antonin Leblanc, Nicolas Mercier, Magali Allain, Jens Dittmer, Thierry Pauporté, et al.. Enhanced Stability and Bangap Tuning of  $\alpha$ -[HC(NH<sub>2</sub>)<sub>2</sub>]PbI<sub>3</sub> Hybrid Perovskite by Large Cation Integration. ACS Applied Materials & Interfaces, 2019, 11 (23), pp.20743-20751. 10.1021/acsami.9b00210 . hal-02127286

**HAL Id: hal-02127286**

**<https://hal.science/hal-02127286>**

Submitted on 1 Jul 2019

**HAL** is a multi-disciplinary open access archive for the deposit and dissemination of scientific research documents, whether they are published or not. The documents may come from teaching and research institutions in France or abroad, or from public or private research centers.

L'archive ouverte pluridisciplinaire **HAL**, est destinée au dépôt et à la diffusion de documents scientifiques de niveau recherche, publiés ou non, émanant des établissements d'enseignement et de recherche français ou étrangers, des laboratoires publics ou privés.

# Enhanced stability and bandgap tuning of $\alpha$ -[HC(NH<sub>2</sub>)<sub>2</sub>]PbI<sub>3</sub> Hybrid Perovskite by Large Cation Integration.

Antonin Leblanc,<sup>a</sup> Nicolas Mercier,<sup>\*a</sup> Magali Allain,<sup>a</sup> Jens Dittmer,<sup>b</sup> Thierry Pauporté,<sup>c</sup>

Vincent Fernandez,<sup>d</sup> Florent Boucher,<sup>d</sup> Mikael Kepenekian,<sup>e</sup> Claudine Katan<sup>\*e</sup>

<sup>a</sup> MOLTECH-ANJOU, UMR-CNRS 6200, Université d'Angers, 2 Bd Lavoisier, 49045 Angers, France.

<sup>b</sup> Institut des Molécules et Matériaux du Mans, CNRS UMR 6283, Le Mans Université, Avenue Olivier Messiaen, 72085 Le Mans cedex 9, France

<sup>c</sup> Chimie ParisTech, PSL Research University, CNRS, Institut de Recherche de Chimie Paris (IRCP), 11 rue P. et M. Curie, F-75005 Paris, France.

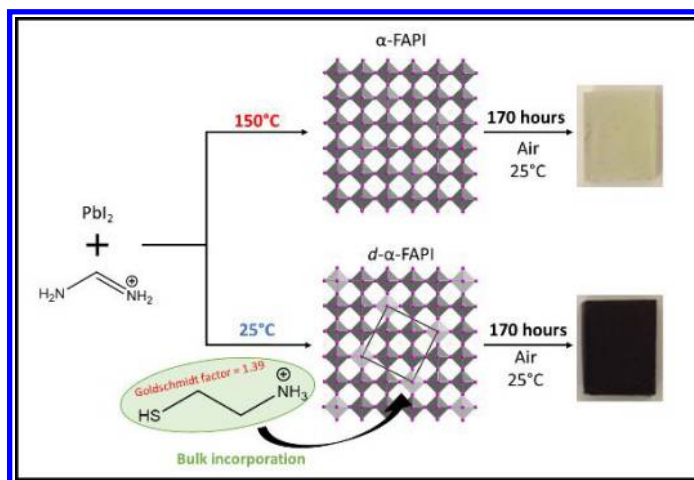
<sup>d</sup> Institut des Matériaux Jean Rouxel, UMR-CNRS 6502, Université de Nantes, 2 rue de la Houssinière, BP 32229, 44322 Nantes Cedex 3, France

<sup>e</sup> Univ Rennes, ENSCR, INSA Rennes, CNRS, ISCR (Institut des Sciences Chimiques de Rennes) - UMR 6226, F-35000 Rennes, France

**Keywords:** halogenated perovskite, Goldschmidt factor, iodoplumbate, formamidinium, alpha-FAPI, lead deficient perovskite, 3D hybrid perovskite

## ABSTRACT

We report room temperature synthesis of lead and iodide deficient  $\alpha$ -[HC(NH<sub>2</sub>)<sub>2</sub>]PbI<sub>3</sub> perovskites (abbreviated  $d$ - $\alpha$ -FAPI, FA<sup>+</sup> = formamidinium), owning the general formula



(A',FA)<sub>1+x</sub>[Pb<sub>1-x</sub>I<sub>3-x</sub>] (with A' = hydroxyethylammonium (HEA<sup>+</sup>) or thioethylammonium

(TEA<sup>+</sup>) cations,  $0.04 \leq x \leq 0.15$ ). These materials retain a 3D character of their perovskite network despite incorporation of large HEA<sup>+</sup> or TEA<sup>+</sup> cations, demonstrating that the Goldschmidt tolerance factor can be bypassed. We found that thin films of (TEA,FA)<sub>1+x</sub>[Pb<sub>1-x</sub>I<sub>3-x</sub>] ( $x = 0.04$  and  $0.13$ ) show exceptional  $\alpha$ -phase stability under ambient conditions, one order of magnitude higher compared to  $\alpha$ -FAPbI<sub>3</sub> and  $\alpha$ -(Cs,FA)PbI<sub>3</sub> thin films. *d*- $\alpha$ -FAPbI<sub>3</sub> phases are shown to maintain a direct bandgap, which increases monotonously for  $x$  ranging from 0 up to 0.20, with characteristics of a p-type semiconductor for low concentrations of vacancies ( $x \leq 0.13$ ) and n-type for larger ones. They offer an alternative to reach methylammonium- and bromine-free stable  $\alpha$ -FAPbI<sub>3</sub> type phase, and open new avenues in the field of perovskite solar cells, up to bandgap tuning desirable for tandem solar cells.

## INTRODUCTION

Since 2012, perovskite based solar cells (PSCs) have shown an impressive potential, combining advantages of low-temperature thin film processing (cost process less than half of the price of c-Si solar cell technology),<sup>1,2</sup> a high power conversion efficiency (PCE) certified up to 23.7%,<sup>3,4</sup> and the possibility of recycling the solar cells.<sup>5,6</sup> However, the well-known (CH<sub>3</sub>NH<sub>3</sub>)PbI<sub>3</sub> hybrid perovskite (abbreviated MAPbI<sub>3</sub>, with MA<sup>+</sup> = methylammonium) firstly used in PSC has shown a fast degradation under air exposure that hinders market development.<sup>7</sup> Consequently, a chemical approach has been applied consisting in substituting the MA<sup>+</sup> cation with a less hydrophilic one, presenting a Goldschmidt tolerance factor in the 0.8-1.0 range suitable for the perovskite phase.<sup>8</sup> Formamidinium (FA<sup>+</sup>) has been considered as a good candidate since the Goldschmidt factor of FAPbI<sub>3</sub> (called FAPbI<sub>3</sub>), is close to 1.0.<sup>8</sup> Unfortunately, the perovskite  $\alpha$ -FAPbI<sub>3</sub>

1  
2  
3 phase, which possesses a better thermal stability and a more suitable bandgap than MAPI,<sup>9</sup>  
4  
5 is only synthesized and is thermodynamically stable beyond 150°C. When cooling down  
6  
7 to room temperature under ambient atmosphere,  $\alpha$ -FAPbI<sub>3</sub> rapidly transforms into  $\delta$ -FAPbI<sub>3</sub>,  
8  
9 an undesirable polymorph phase that does not present a perovskite architecture nor  
10  
11 photoactivity.<sup>10</sup> In order to slow down this  $\alpha$ -to- $\delta$  phase transformation, a double cation  
12  
13 strategy was first developed. This chemical approach consists of the  $\alpha$ -phase stabilisation  
14  
15 by mixing two materials possessing a large and a small Goldschmidt tolerance factors,  
16  
17 leading to an alloy which owns a balanced factor comprised between the suitable range  
18  
19 [0.8 - 1.0]. The resulting two archetype compounds are Cs<sub>0.15</sub>FA<sub>0.85</sub>PbI<sub>3</sub> and  
20  
21 MA<sub>0.20</sub>FA<sub>0.80</sub>PbI<sub>3</sub>.<sup>11,12</sup> This strategy was successful as the  $\alpha$ -to- $\delta$  phase transformation was  
22  
23 observed after a longer time (air condition) than with  $\alpha$ -FAPbI<sub>3</sub>, and improved efficiencies  
24  
25 for solar cells were also achieved. Subsequently, other combinations of multiple cations  
26  
27 and mixed halide were employed, leading to the most stable and efficient alloys  $\alpha$ -  
28  
29 (Rb/Cs/MA)<sub>0.20-0.25</sub>FA<sub>0.75-0.80</sub>Pb(I<sub>0.85</sub>Br<sub>0.15</sub>)<sub>3</sub>, regularly exceeding 20% solar cells.<sup>13-20</sup>  
30  
31 However, despite the beneficial effects of the presence of MA<sup>+</sup> and Br<sup>-</sup> ions on the  $\alpha$ -phase  
32  
33 purity, crystallinity, stability and on solar cell efficiencies, both volatile MA<sup>+</sup> cation and  
34  
35 Br<sup>-</sup> halide induce thermal degradation and an unsuitable blue-shift of the bandgap.<sup>21</sup>  
36  
37 Moreover, from a chemical point of view, this multi-cations alloying strategy is still sorely  
38  
39 limited by the choice of the cations that possess a suitable size to keep a 3D perovskite  
40  
41 architecture.  
42  
43  
44  
45  
46  
47  
48

49 Recently, we have reported unprecedented lead and iodide deficient hybrid perovskite  
50  
51 materials (*d*-HP family), owning a general formulation (A')<sub>3.48x</sub>(A)<sub>1-2.48x</sub>[Pb<sub>1-x</sub>I<sub>3-x</sub>], where  
52  
53 A = MA<sup>+</sup> and A' = HEA<sup>+</sup> (hydroxyethylammonium HO-(CH<sub>2</sub>)<sub>2</sub>-NH<sub>3</sub><sup>+</sup>).<sup>22</sup> The resulting  
54  
55

1  
2  
3 phases, named *d*-MAPI, present a 3D perovskite corner-shared  $\text{Pb}_{1-x}\text{I}_{3-x}$  ( $x = 0$  to  $0.20$ )  
4 network, which can be described as a lead and iodide deficient  $\text{PbI}_3$  MAPI network. A  
5 slightly improved air stability has been demonstrated for this *d*-MAPI phases as compared  
6 to MAPI.<sup>22</sup> More recently, Diau *et al.* have prepared the tin analogue (*d*-(MA)SnI<sub>3</sub>) which  
7 also shows good air stability.<sup>23</sup> This superior air stability was also observed for the *hollow*  
8 hybrid perovskites named (A',A)MI<sub>3</sub> (A' = en<sup>2+</sup> = ethylenediammonium, A = MA<sup>+</sup>/FA<sup>+</sup>, M  
9 = Pb<sup>2+</sup>/Sn<sup>2+</sup>) reported by the Kanatzidis' group.<sup>24</sup> When A = FA<sup>+</sup>, a series of *hollow*  
10 perovskites are obtained: (FA)<sub>1-x</sub>(en)<sub>x</sub>Pb<sub>0.7x</sub>I<sub>3-0.4x</sub>. However, they are synthesized at  
11 temperatures over 100 °C, as the  $\alpha$ -FAPI phase, and no thin film preparation (and so no  
12 thin film stability test) of these *hollow- $\alpha$* -FAPI phases has been reported.<sup>24</sup>

13  
14  
15  
16  
17  
18  
19  
20  
21  
22  
23  
24  
25  
26 In this study, we report the room temperature synthesis of a family of lead and iodide  
27 deficient  $\alpha$ -FAPI (*d- $\alpha$* -FAPI) hybrid perovskites. These 3D perovskites incorporate the  
28 formamidinium cation and a larger size cation, either the hydroxyethylammonium (HEA<sup>+</sup>,  
29 *d- $\alpha$* -FAPI-**H**<sub>x</sub> compounds) or the thioethylammonium (TEA<sup>+</sup>, *d- $\alpha$* -FAPI-**T**<sub>x</sub> compounds)  
30 monocation. The general formula of these materials is (FA,A')<sub>1+x</sub>[Pb<sub>1-x</sub>I<sub>3-x</sub>] with A' = HEA<sup>+</sup>  
31 or TEA<sup>+</sup>. Crystals of *d- $\alpha$* -FAPI have been grown, allowing the selection and structure  
32 determination of one composition, (HEA)<sub>0.406</sub>(FA)<sub>0.698</sub>[Pb<sub>0.896</sub>I<sub>2.896</sub>] ( $x = 0.104$ , written *d- $\alpha$* -  
33 *FAPI-**H***<sub>0.104</sub>), which revealed the 3D nature of the perovskite network. Several materials  
34 have been also prepared as pure crystallized powder phases, two *d- $\alpha$* -FAPI-**H**<sub>x</sub> (with  $x =$   
35  $0.13$  and  $x = 0.15$ , here abbreviated **H**<sub>0.13</sub>, and **H**<sub>0.15</sub>), and one *d- $\alpha$* -FAPI-**T**<sub>x</sub> ( $x = 0.04$ ,  
36 abbreviated **T**<sub>0.04</sub>), as well as thin films (**H**<sub>0.13</sub>, **H**<sub>0.15</sub>, **T**<sub>0.04</sub> and also **T**<sub>0.13</sub> ( $x = 0.13$ )).  
37  
38  
39  
40  
41  
42  
43  
44  
45  
46  
47  
48  
49  
50  
51  
52  
53  
54  
55  
56  
57  
58  
59  
60

1  
2  
3 visible absorption and X-ray photoelectron spectroscopy (XPS) measurements. Moreover,  
4 the analysis has been completed by computational DFT investigations. Besides the fact that  
5 these  $\alpha$ -FAP<sub>x</sub> type phases can be synthesized at room temperature, we show that the  
6 stability of the  $\alpha$  phase at room temperature and under ambient condition (thin films, case  
7 of  $d$ - $\alpha$ -FAP<sub>x</sub>-T<sub>x</sub> materials) is exceptionally improved compared to both  $\alpha$ -FAP<sub>x</sub> and  $\alpha$ -  
8 Cs<sub>0.15</sub>FA<sub>0.85</sub>PbI<sub>3</sub> reference materials.  
9  
10  
11  
12  
13  
14  
15  
16  
17  
18

## 19 RESULTS AND DISCUSSION

20 Crystals of  $d$ - $\alpha$ -FAP<sub>x</sub> have been obtained at room temperature by slow liquid-gas diffusion  
21 process using aqueous hydroiodic acid and ethanol as solvent and anti-solvent, respectively  
22 (more details in Supporting Information -I.a-). These crystals have a cross shape (Figure  
23 **1a**), and depending on experimental conditions they can be black or dark red. It is also  
24 worth noting that no yellow crystals of  $\delta$ -FAP<sub>x</sub> were co-crystallized. For all  $x$  values ,  
25 single-crystal X-ray diffraction analysis of  $d$ - $\alpha$ -FAP<sub>x</sub>-H<sub>x</sub> has revealed room temperature  
26 tetragonal unit cells ( $a = b = 14.471 \text{ \AA}$ ,  $c = 6.448 \text{ \AA}$ ,  $\alpha = \beta = \gamma = 90^\circ$ ,  $V = 1350.2 \text{ \AA}^3$ ),  
27 slightly larger than the previously reported  $d$ -MAP<sub>x</sub> unit cell (also obtained at room  
28 temperature:  $a = b = 14.312 \text{ \AA}$ ,  $c = 6.366 \text{ \AA}$ ,  $\alpha = \beta = \gamma = 90^\circ$ ,  $V = 1303.9 \text{ \AA}^3$ ).<sup>22</sup> This can be  
29 correlated to the effective radius of FA<sup>+</sup> (253 pm) which is larger than the one of MA<sup>+</sup> (217  
30 pm).<sup>25</sup> The structure of the  $d$ - $\alpha$ -FAP<sub>x</sub>-H<sub>x</sub> was studied from one single crystal selected  
31 among many other. The  $d$ - $\alpha$ -FAP<sub>x</sub>-H<sub>x</sub> phase crystallises at room temperature into the P4/m  
32 space group (see S.I. IV, Table S7). Despite several attempts at different temperatures (100-  
33 293K range), the X-ray study has only allowed the determination of the inorganic network.  
34  
35  
36  
37  
38  
39  
40  
41  
42  
43  
44  
45  
46  
47  
48  
49  
50  
51  
52  
53  
54 This can be partly explained at room temperature by a dynamical disorder of both HEA<sup>+</sup>  
55  
56  
57  
58  
59  
60

1  
2  
3 and FA<sup>+</sup> organic cations, as revealed by solid state NMR experiments (see below). At lower  
4  
5 temperature, this may be explained by a statistical disorder. Structural refinements finally  
6  
7 led to a Pb<sub>4.48</sub>I<sub>14.48</sub> formula per unit cell for the inorganic part. The structure can be  
8  
9 described from a main 3D Pb<sub>4</sub>I<sub>14</sub> perovskite network of corner-sharing PbI<sub>6</sub> octahedra with  
10  
11 a 3D arrangement which generates channels along the *c* axis (Figure 1b). These channels  
12  
13 are half filled with extra Pb<sup>2+</sup> and I<sup>-</sup> ions, located in (0, 0, 0) and (0, 0, 0.5), respectively.  
14  
15 To highlight the lead and iodide deficiency of this 3D perovskite network, the Pb<sub>4.48</sub>I<sub>14.48</sub>  
16  
17 formula should be written as Pb<sub>0.896</sub>I<sub>2.896</sub> or Pb<sub>1-x</sub>I<sub>3-x</sub> with *x* = 0.104 (*d*-α-FAPI-**H**<sub>0.104</sub>). The  
18  
19 general formulation of the *d*-α-FAPI-**H**<sub>*x*</sub> phases is (HEA)<sub>3.9*x*</sub>(FA)<sub>1-2.9*x*</sub>[Pb<sub>1-x</sub>I<sub>3-x</sub>] or  
20  
21 (HEA,FA)<sub>1+x</sub>[Pb<sub>1-x</sub>I<sub>3-x</sub>] according to different chemical analyses of crystals and powders  
22  
23 (see below and S.I.) and therefore the formula of this studied crystal is  
24  
25 (HEA)<sub>0.406</sub>(FA)<sub>0.698</sub>[Pb<sub>0.896</sub>I<sub>2.896</sub>]. Thus, the lead and iodide deficient *d*-α-FAPI phase can  
26  
27 be described from the α-FAPI phase through a substitution of *x* (PbI)<sup>+</sup> units by *x* organic  
28  
29 cations, HEA<sup>+</sup> or FA<sup>+</sup>. In the case of *x* = 0.2 (Pb<sub>0.8</sub>I<sub>2.8</sub> or Pb<sub>4</sub>I<sub>14</sub> network), all Pb<sup>2+</sup> and I<sup>-</sup> ions  
30  
31 along the *c* direction have been substituted by organic cations leading to empty channels.  
32  
33 When 0 ≤ *x* ≤ 0.2 (case of the studied crystal *d*-α-FAPI-**H**<sub>0.104</sub>), the X-ray analysis shows  
34  
35 that channels contain Pb<sup>2+</sup> and I<sup>-</sup> anions as well as organic cations. Consequently, one  
36  
37 hypothesis is a partial filling of channels by Pb<sup>2+</sup> and I<sup>-</sup>. Another hypothesis is that  
38  
39 intermediate values of *x* may correspond to a limited number of empty channels in the  
40  
41 structure (see below the model structures used for calculations). Finally, it must be noted  
42  
43 that the poor quality of crystals of *d*-α-FAPI-**T**<sub>*x*</sub> precluded their X-ray single crystal  
44  
45 analysis.  
46  
47  
48  
49  
50  
51  
52  
53  
54  
55  
56  
57  
58  
59  
60

1  
2  
3 From the crystal structure analysis of the anhydrous iodide salts of  
4 hydroxyethylammonium (HEAI) and thioethylammonium (TEAI) which have revealed  
5 that HEA<sup>+</sup> and TEA<sup>+</sup> cations adopt a curving shape (S.I. Tables S8 and S9), we estimated  
6 the effective radius of HEA<sup>+</sup> (3.44 Å) and TEA<sup>+</sup> (4.14 Å) according to the model proposed  
7 by Kieslich *et al.*<sup>25</sup> Thus, the Goldschmidt factors of the hypothetical (HEA)PbI<sub>3</sub> and  
8 (TEA)PbI<sub>3</sub> perovskites were calculated as 1.24 and 1.39, respectively. These values are far  
9 from the expected 0.8-1.0 range usually necessary to stabilize the 3D ABX<sub>3</sub> perovskite.<sup>8</sup>  
10 However, the 3D perovskite structures of  $\alpha$ -FAPI type prepared in this work (*d*- $\alpha$ -FAPI  
11 phases) have been stabilized despite the incorporation of these HEA<sup>+</sup> / TEA<sup>+</sup> cations (see  
12 below). This is explained by the presence of (PbI)<sup>+</sup> vacancies in the 3D network. This  
13 family of compounds (*d*-HP) shows that it is possible to circumvent the geometrical  
14 Goldschmidt factor and to obtain 3D hybrid perovskites even using larger R-NH<sub>3</sub><sup>+</sup> organic  
15 cations. Moreover, the integration of HEA<sup>+</sup>/TEA<sup>+</sup> cation allows the synthesis at room  
16 temperature of the  $\alpha$ -FAPI type network (*d*- $\alpha$ -FAPI) while  $\alpha$ -FAPI reference is prepared  
17 only at temperature over 150 °C.  
18  
19  
20  
21  
22  
23  
24  
25  
26  
27  
28  
29  
30  
31  
32  
33  
34  
35  
36  
37  
38  
39  
40  
41  
42  
43  
44  
45  
46  
47  
48  
49  
50  
51  
52  
53  
54  
55  
56  
57  
58  
59  
60



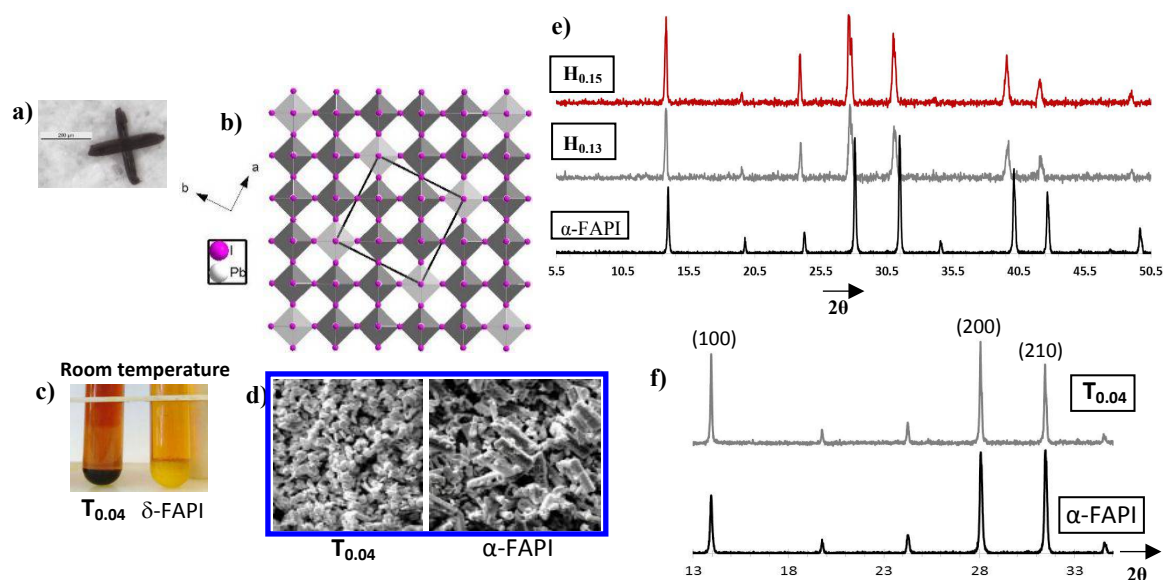


**Figure 1.** *a)* Cross-shaped crystals of  $d$ - $\alpha$ -FAPIs. *b)* View along the  $c$  axis of the tetragonal unit cell (black square) of the structure of  $(\text{HEA,FA})_{1.104}[\text{Pb}_{0.896}\text{I}_{2.896}]$  showing the lead and iodide deficient perovskite network (dark grey octahedra : full  $\text{Pb}^{2+}$  and I sites occupancy, light grey octahedra: half  $\text{Pb}^{2+}$  and I sites occupancy). *c)* Photography of  $T_{0.04}$  and  $\delta$ -FAPIs synthesized at room temperature; *d)* SEM images of crystallized powders of  $T_{0.04}$  and  $\alpha$ -FAPIs; *e)* XRD patterns of  $H_{0.13}$ ,  $H_{0.15}$  and  $\alpha$ -FAPIs showing the shift of lines towards low angles for  $H_{0.13}$  and  $H_{0.15}$ ; *f)* XRD patterns of  $T_{0.04}$  and  $\alpha$ -FAPIs highlighting the (100), (200) and (210) diffraction lines.

Powders of  $d$ - $\alpha$ -FAPIs- $H_x$  and  $d$ - $\alpha$ -FAPIs- $T_x$  were prepared by a fast precipitation method at room temperature. Increasing amounts of hydroxyethylamine/FAI/ $\text{PbI}_2$  or thioethylamine/FAI/ $\text{PbI}_2$  were dissolved at room temperature into aqueous hydroiodic acid under ultrasonication until the saturation was reached. Then, the saturated solution was

1  
2  
3 poured into ethyl acetate, immediately leading to the precipitation of a powder (more  
4 details in S.I. I.b). Pure *d*- $\alpha$ -FAPI- $\mathbf{H}_x$  phases with  $x = 0.13$  ( $\mathbf{H}_{0.13}$ ) and  $x = 0.15$  ( $\mathbf{H}_{0.15}$ ), as  
5 well as one pure phase of *d*- $\alpha$ -FAPI- $\mathbf{T}_x$  with  $x = 0.04$  ( $\mathbf{T}_{0.04}$ ), were obtained and fully  
6 characterized. We also prepared the  $\delta$ -FAPI by starting from  $\text{PbI}_2$  and FAI as reagents, and  
7 also synthesized  $\alpha$ -FAPI compound by heating the  $\delta$ -FAPI powder at 155°C during 30 min.  
8 A color change then occurs from yellow to black characterizing the  $\delta$ -FAPI to  $\alpha$ -FAPI  
9 phase transition. Despite our best efforts to precipitate pure phases with compositions in  
10 the  $x = 0$ -0.20 range, only one composition could be obtained for *d*- $\alpha$ -FAPI- $\mathbf{T}_x$  ( $\mathbf{T}_{0.04}$ ) while  
11 two distinct compositions ( $\mathbf{H}_{0.13}$  and  $\mathbf{H}_{0.15}$ ) were obtained with  $\text{HEA}^+$ . In all other  
12 experiments, the yellow  $\delta$ -FAPI was crystallized as impurity. Figure 1c (zoomed Figure  
13 S7) shows a photography of  $\delta$ -FAPI and  $\mathbf{T}_{0.04}$  precipitated powders.  $\delta$ -FAPI powder has a  
14 typical yellow color while the  $\mathbf{T}_{0.04}$  powder is black, showing that another phase is obtained  
15 when a small amount of  $\text{TEA}^+$  is incorporated in the system, which will be proved to be a  
16  $\alpha$ -FAPI type phase (*d*- $\alpha$ -FAPI). Furthermore, it is worth noting that the morphology of  $\alpha$ -  
17 FAPI and  $\mathbf{T}_{0.04}$  micrometer-size crystals (obtained by the precipitation method) are very  
18 different, as shown by scanning electron microscopy images (Figure 1d, zoomed Figure  
19 S8). Indeed, the elongated shape of  $\alpha$ -FAPI crystals is the consequence of the preferential  
20 growth along the  $\text{PbI}_3^-$  chain direction of the initial  $\delta$ -FAPI compound,<sup>10</sup> while a cube shape  
21 is observed for  $\mathbf{T}_{0.04}$  crystals proving that the cubic  $\alpha$ -FAPI type network was directly  
22 obtained.  $\mathbf{H}_{0.13}$ ,  $\mathbf{H}_{0.15}$  and  $\mathbf{T}_{0.04}$  samples have been fully characterized, first by energy  
23 dispersive X-ray spectroscopy (EDX) allowing the determination of the I/Pb atomic ratios.  
24 Considering the inorganic network  $[\text{Pb}_{1-x}\text{I}_{3-x}]$  as found in the *d*-MAPI phases  
25 ( $\text{HEA,MA})_{1+x}[\text{Pb}_{1-x}\text{I}_{3-x}]$ ,<sup>22</sup> and in this studied crystal  $\mathbf{H}_{0.104}$  ( $\text{Pb}_{0.896}\text{I}_{2.896}$  network,  $x = 0.104$ ),  
26  
27  
28  
29  
30  
31  
32  
33  
34  
35  
36  
37  
38  
39  
40  
41  
42  
43  
44  
45  
46  
47  
48  
49  
50  
51  
52  
53  
54  
55

1  
2  
3 the measured I/Pb atomic ratios gave  $x = 0.13$  for  $\mathbf{H}_{0.13}$ ,  $x = 0.15$  for  $\mathbf{H}_{0.15}$ , and  $x = 0.04$  for  
4  $\mathbf{T}_{0.04}$  (Figures S1, S8, and Tables S3, S6). Moreover,  $^1\text{H}$  nuclear magnetic resonance  
5 spectroscopy (NMR) in solution led to determine the following  $\text{HEA}^+/\text{FA}^+$  and  $\text{TEA}^+/\text{FA}^+$   
6 molecular ratios:  $\text{HEA}^+/\text{FA}^+ = 0.81$  for  $\mathbf{H}_{0.13}$  and  $1.13$  for  $\mathbf{H}_{0.15}$ , and  $\text{TEA}^+/\text{FA}^+ = 0.13$  for  
7  $\mathbf{T}_{0.04}$  (Figures S2-S6, S9-11). The following formulations were thus deduced:  
8  $(\text{HEA})_{0.51}(\text{FA})_{0.62}[\text{Pb}_{0.87}\text{I}_{2.87}]$  ( $\mathbf{H}_{0.13}$ ) and  $(\text{HEA})_{0.60}(\text{FA})_{0.55}[\text{Pb}_{0.85}\text{I}_{2.85}]$  ( $\mathbf{H}_{0.15}$ ), consistent  
9 with the general formulation of  $(\text{HEA})_{3.9x}(\text{FA})_{1-2.9x}[\text{Pb}_{1-x}\text{I}_{3-x}]$ , with  $x = 0.13$  and  $x = 0.15$ ;  
10 and  $(\text{TEA})_{0.12}(\text{FA})_{0.92}[\text{Pb}_{0.96}\text{I}_{2.96}]$  ( $\mathbf{T}_{0.04}$ ,  $x = 0.04$ ). All these compositions were finally  
11 confirmed by elemental analysis (Tables S1, S2, S4, and S5). The purity of all these  
12 crystallized powders was also verified by powder X-ray diffraction (XRD) analysis. The  
13 XRD patterns of the yellow  $\delta$ -FAPI and the black  $\alpha$ -FAPI powders (Figures S12 and S13)  
14 perfectly fit with their theoretical XRD patterns, calculated from both known  $\delta$ -FAPI and  
15  $\alpha$ -FAPI structures ( $\delta$ -FAPI: hexagonal  $\text{P6}_3\text{mc}$ ,  $a = b = 8.7 \text{ \AA}$ ,  $c = 7.9 \text{ \AA}$ ;  $\alpha$ -FAPI: cubic  $\text{Pm-}$   
16  $3\text{m}$ ,  $a = 6.362 \text{ \AA}$  for).<sup>10,26</sup>

17  
18  
19  
20  
21  
22  
23  
24  
25  
26  
27  
28  
29  
30  
31  
32  
33  
34  
35 As regards  $\mathbf{H}_{0.13}$  and  $\mathbf{H}_{0.15}$  powders, their XRD patterns are in good agreement with the  
36 calculated XRD pattern from the single crystal data of  $(\text{HEA,FA})_{1.104}[\text{Pb}_{0.896}\text{I}_{2.896}]$  (Figure  
37 S14). In Figure 1e, diffractograms of  $\mathbf{H}_{0.13}$ ,  $\mathbf{H}_{0.15}$  and  $\alpha$ -FAPI powders are provided.  
38 Compared to  $\alpha$ -FAPI, a slight shift of most peaks of  $\mathbf{H}_{0.13}$  and  $\mathbf{H}_{0.15}$  towards lower angles  
39 is observed (see also zoom in Figure S15). This phenomenon, revealing a slight increase  
40 of unit cell parameters through the substitution process of  $(\text{PbI})^+$  units by organic cations,  
41 has been already observed in the case of  $d$ -MAPI phases  $(\text{HEA,MA})_{1+x}[\text{Pb}_{1-x}\text{I}_{3-x}]$ .<sup>22</sup> Three  
42 peaks of low intensity which were expected at low  $2\theta$  angles ( $6.2^\circ$ ,  $8.7^\circ$ ,  $12.3^\circ$ ) are absent  
43 in the XRD patterns of  $\mathbf{H}_{0.13}$  and  $\mathbf{H}_{0.15}$  (Figure 1e and Figure S14 -theoretical XRD pattern-  
44  
45  
46  
47  
48  
49  
50  
51  
52  
53  
54  
55

1  
2  
3 ). These lines are assigned to (1 0 0), (1 1 0) and (2 0 0) planes of the tetragonal unit cell  
4  
5 (a = 14.312 Å, c = 6.366 Å) typical of the *d*-HP phase<sup>22</sup> (see Figure 1b). The fact that these  
6  
7 lines are not observed could be explained by a preferential orientation phenomenon of (0  
8  
9 0 l) type, but most probably the smaller unit cell observed is resulting of a non-ordered  
10  
11 distribution of defaults (lead and iodide vacancies) as observed in *hollow* structures based  
12  
13 on ethylenediammonium cations.<sup>24</sup> Unlike the *d*- $\alpha$ -FAPI- $\mathbf{H}_x$  phases, the XRD pattern of  
14  
15  $\mathbf{T}_{0.04}$  does not present significant shifts compared to the  $\alpha$ -FAPI XRD one (Figures 1f, S16).  
16  
17 This may be explained by the low incorporation of TEA<sup>+</sup> cations into this  $\mathbf{T}_{0.04}$  phase (x=  
18  
19 0.04, TEA/FA= 0.13). Nevertheless, we can notice differences for several diffraction peak  
20  
21 intensities. Thus, the intensities I(100)/I(200) ratio ((100) line at 13.9° and (200) line at  
22  
23 28.0°) appears higher in  $\mathbf{T}_{0.04}$  than in  $\alpha$ -FAPI, and this cannot be explained by a preferential  
24  
25 orientation phenomenon. We also notice that I(210) ((210) line at 31.4°) is lowered in  $\mathbf{T}_{0.04}$   
26  
27 compared to  $\alpha$ -FAPI. This feature is probably the consequence of a slight structural  
28  
29 modification involved by the incorporation of TEA<sup>+</sup> in  $\mathbf{T}_{0.04}$ . Moreover, this phenomenon  
30  
31 is also observed when materials ( $\mathbf{T}_{0.04}$ ,  $\mathbf{T}_{0.13}$ , and  $\alpha$ -FAPI) are prepared as thin films (see  
32  
33 below).  
34  
35  
36  
37  
38  
39  
40  
41  
42  
43  
44  
45  
46  
47  
48  
49  
50  
51  
52  
53  
54  
55  
56  
57  
58  
59  
60

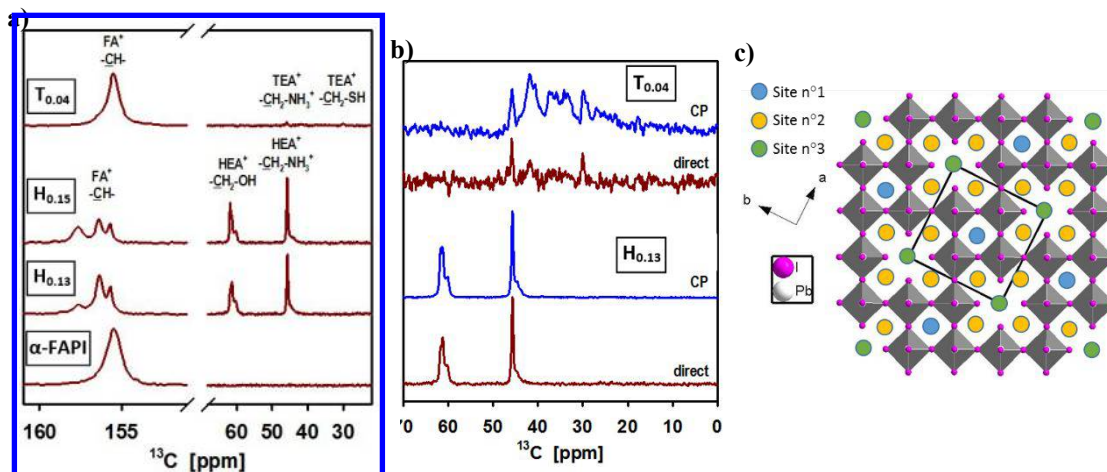


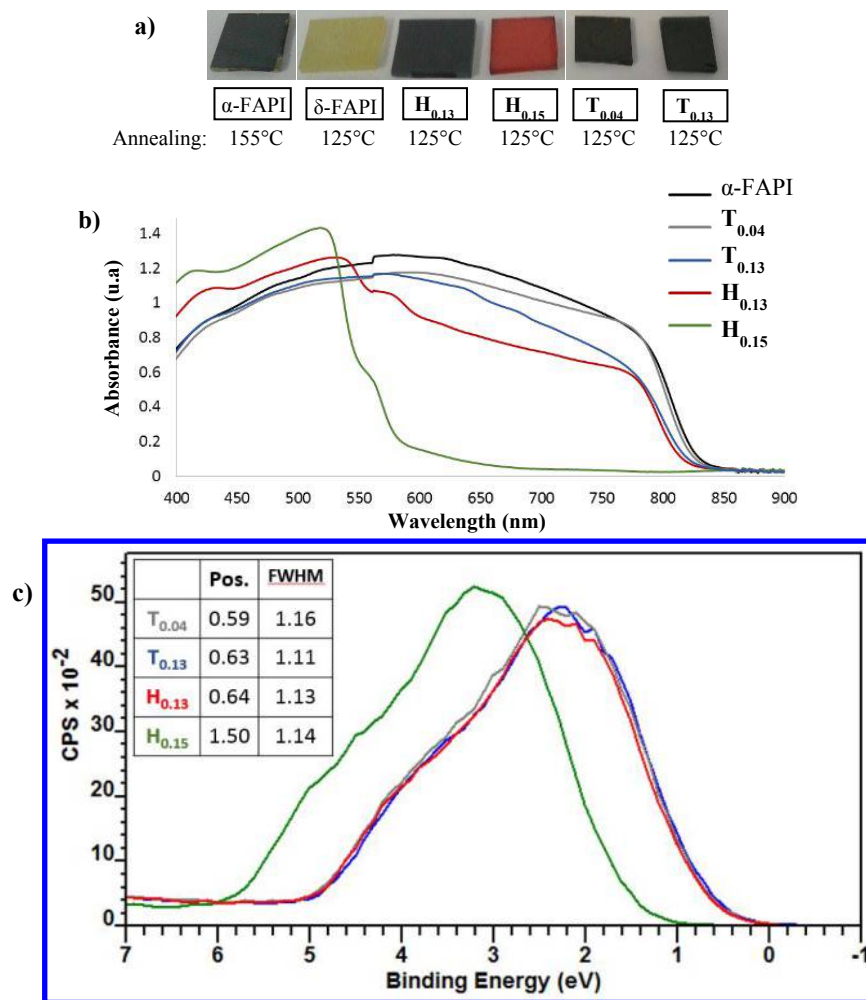
**Figure 2.** *a)* Direct excitation solid state NMR spectra of  $\alpha$ -FAPI,  $H_{0.13}$ ,  $H_{0.15}$ , and  $T_{0.04}$ , scaled according to the number of scans. *b)* The upfield region of the direct excitation spectra (red) of  $H_{0.13}$  and  $T_{0.04}$  compared to the corresponding cross polarization spectra (blue). Arbitrary scale. *c)* View along the  $c$  axis of the tetragonal unit cell (black square) of a hypothetical structure of  $d$ - $\alpha$ -FAPI with  $x = 0.20$  (resulting formula of (HEA or TEA, FA) $_{1.2}$ [Pb $_{0.8}$ I $_{2.8}$ ]). The organic cations are located on the three different crystallographic site  $n^{\circ}1$ ,  $n^{\circ}2$  and  $n^{\circ}3$  (blue, yellow and green circles, respectively).

$^{13}\text{C}$  solid state NMR was used to characterize the organic cations, invisible to XRD, verify their incorporation into the perovskite framework and gain information on their dynamics. While the direct excitation  $^{13}\text{C}$  spectrum of  $\alpha$ -FAPI shows the expected single signal of the  $\text{FA}^+$  carbon (at 155.5 ppm), the materials  $H_{0.13}$  and  $H_{0.15}$  show two additional signals around 61 and 45 ppm, corresponding to  $-\text{CH}_2-\text{OH}$  and of  $-\text{CH}_2-\text{NH}_3^+$  of the  $\text{HEA}^+$  cation, respectively (Figure 2a). Concerning the  $\text{FA}^+$  signal, it shifts upon the insertion of the other cations, similar to  $\text{MA}^+$  in  $d$ -MAPI phases,<sup>22</sup> but also splits into three signals, at identical

positions for  $\mathbf{H}_{0.13}$  and  $\mathbf{H}_{0.15}$ . These observations are consistent with the possible occupation of different sites in this lead and iodide deficient perovskite network: three sites for the  $\text{FA}^+$  ions, and probably only the sites  $n^\circ 2$  and  $n^\circ 3$  for  $\text{HEA}^+$  ions (see below Figure **2c**). The least shifted (0.2 compared to 0.9 and 2.2 ppm) signal is here most likely from  $\text{FA}^+$  on the site corresponding to the unmodified FAPI structure (site  $n^\circ 1$ ). There is also dispersion in the  $\text{HEA}^+$  signals: both signals in both samples consist of a dominant peak on the downfield side, interpreted as stemming from  $\text{HEA}^+$  on the more abundant site  $n^\circ 2$ , and a broader foot upfield, attributed to  $\text{HEA}^+$  on site  $n^\circ 3$ . The chemical shift range of the latter contains the shift of HEAI, because the local environment of the carbons on site  $n^\circ 3$  is closer to those in HEAI (Figure S22). The  $\text{HEA}^+$  signals show substructures, in particular the foot of  $-\text{CH}_2-\text{NH}_3^+$  on site  $n^\circ 3$ , indicating that these cations are not all incorporated in the same way or that there are preferential orientations. In fact,  $^{13}\text{C}$  cross-polarization (CP) spectra of  $\mathbf{H}_{0.13}$  and  $\mathbf{H}_{0.15}$  exhibit intense signals compared to  $\alpha$ -FAPI showing that the free rotation of the cations is restrained by the structure (Figure S22). This counts in particular for the bigger  $\text{HEA}^+$  cations. It is thus imaginable that there are preferred orientations that have lifetimes being long enough that the NMR signals are not fully averaged.

For  $\mathbf{T}_{0.04}$ , the  $\text{CH}_2$   $^{13}\text{C}$  signals of  $\text{TEA}^+$  are hardly detectable by a direct excitation experiment. Their shifts are 45.9 and 30.3 ppm, respectively, different from those of TEAI (Figure S22). The  $^{13}\text{C}$  CP experiment reveals a broad distribution of additional signals in the  $\text{CH}_2$  region (Figure **2b**). Note that this experiment is not quantitative and enhances signals stemming from less mobile molecules or molecule groups. In the direct excitation experiment their intensity is so low that they are largely covered by the noise. Nevertheless, as they are spread over a broader range, they probably constitute the major part of  $\text{TEA}^+$ .

1  
2  
3 (This finding is in contrast to **H<sub>0.13</sub>** and **H<sub>0.15</sub>**, where the shapes of the signals acquired with  
4 CP and direct excitation are essentially identical, indicating that the dynamics of all HEA<sup>+</sup>  
5 is similar (Figure **2b**, **H<sub>0.13</sub>**.) Incorporated TEA<sup>+</sup> thus presents in the majority much less  
6 rotational mobility compared to the other organic cations (FA<sup>+</sup>, HEA<sup>+</sup> in **H<sub>0.13</sub>** and **H<sub>0.15</sub>**).  
7  
8  
9  
10  
11  
12  
13  
14  
15  
16  
17  
18  
19  
20  
21  
22  
23  
24  
25  
26  
27  
28  
29  
30  
31  
32  
33  
34  
35  
36  
37  
38  
39  
40  
41  
42  
43  
44  
45  
46  
47  
48  
49  
50  
51  
52  
53  
54  
55  
56  
57  
58  
59  
60



38 **Figure 3. a)** Photography of  $\alpha$ -FAPl,  $\delta$ -FAPl,  $H_{0.13}$ ,  $H_{0.15}$ ,  $T_{0.04}$  and  $T_{0.13}$  thin films and  
 39 their associated temperatures of annealing. **b)** UV-visible absorbance spectra of  $\alpha$ -FAPl  
 40 (black),  $H_{0.13}$  (red),  $H_{0.15}$  (green),  $T_{0.04}$  (grey), and  $T_{0.13}$  (blue) thin films. **c)** XPS spectra of  
 41  $H_{0.13}$  (red),  $H_{0.15}$  (green),  $T_{0.04}$  (grey) and  $T_{0.13}$  (blue) thin films, representing the valence  
 42 band (VB) energies relative to the Fermi energy ( $E_F - E_{VB}$ ). Inset: respective both energies  
 43 (eV) of  $E_F - E_{VB}$  (pos.) and FWHM.  
 44  
 45  
 46  
 47  
 48  
 49  
 50  
 51  
 52  
 53  
 54  
 55  
 56  
 57  
 58  
 59  
 60



Thin films of  $d$ - $\alpha$ -FAP $\text{I-H}_x$  and  $d$ - $\alpha$ -FAP $\text{I-T}_x$  phases as well as  $\alpha$ -FAP $\text{I}$  were prepared by spin coating at room conditions (see S.I. -I.e- for details). The precursors were added into a solution of dimethylformamide (DMF), and depending on stoichiometries of the reagents, we prepared  $\alpha$ -FAP $\text{I}$  (PbI $_2$ /FAI: 1/1),  $\mathbf{H}_{0.13}$  (PbI $_2$ /FAI/HEAI: 3/3/1),  $\mathbf{H}_{0.15}$  (PbI $_2$ /FAI/HEAI: 3/3/2),  $\mathbf{T}_{0.04}$  (PbI $_2$ /FAI/TEAI: 3/3/0.5), and contrary to the precipitated powders, we were able to prepare another successfully pure composition  $\mathbf{T}_{0.13}$  ( $x = 0.13$ ; PbI $_2$ /FAI/TEAI: 3/3/1.0). The spinning step was followed by an annealing treatment of thin films, at 155°C for  $\alpha$ -FAP $\text{I}$  and at 125°C for  $\mathbf{H}_{0.13}$ ,  $\mathbf{H}_{0.15}$ ,  $\mathbf{T}_{0.04}$ , and  $\mathbf{T}_{0.13}$ . We must notice that the annealing of the FAP $\text{I}$  thin film at 125 °C results in the formation of  $\delta$ -FAP $\text{I}$  as a pure phase (yellow thin film). After the annealing step, thin films of  $\alpha$ -FAP $\text{I}$ ,  $\mathbf{H}_{0.13}$ ,  $\mathbf{T}_{0.04}$ , and  $\mathbf{T}_{0.13}$  are black, and red for  $\mathbf{H}_{0.15}$  (see Figure 3a).

As for powders, the I/Pb ratio of this films were determined from EDX analysis, leading to  $x = 0.13$  ( $\mathbf{H}_{0.13}$ ),  $x = 0.15$  ( $\mathbf{H}_{0.15}$ ) (Figure S1, Table S3),  $x = 0.04$  ( $\mathbf{T}_{0.04}$ ), and  $x = 0.13$  ( $\mathbf{T}_{0.13}$ ) (Figure S8, Table S6). XRD measurements revealed that  $\mathbf{H}_{0.13}$  and  $\mathbf{H}_{0.15}$  thin films were obtained as pure phases without the presence of  $\delta$ -FAP $\text{I}$ ,  $\alpha$ -FAP $\text{I}$  or PbI $_2$ . The XRD patterns of  $\mathbf{H}_{0.13}$  and  $\mathbf{H}_{0.15}$  exhibit a shift of most of peaks towards lower angles compared to the lines of  $\alpha$ -FAP $\text{I}$ , as observed for powders. We also notice that the three very weak peaks at low  $2\theta$  angle (6.2°, 8.7°, 12.3°), typical of the tetragonal super-cell of such  $d$ -HP (see single crystal study) are observed in the thin film pattern of  $\mathbf{H}_{0.15}$  (Figure S17). As in the case of  $d$ - $\alpha$ -FAP $\text{I-H}_x$  phases, XRD patterns of  $\mathbf{T}_{0.04}$  and  $\mathbf{T}_{0.13}$  thin films show single phase layers without the presence of PbI $_2$  (Figure S20). This is in contrast with the XRD of  $\alpha$ -FAP $\text{I}$  thin film (PbI $_2$  is known to be easily generated during the annealing treatment at 155°C -room conditions-) (Figures S18, S19).<sup>27,28</sup> As observed in the XRD of  $\mathbf{T}_{0.04}$  powder and the XRD

1  
2  
3 of ethylene diammonium ( $en^{2+}$ ) based *hollow* perovskites  $(FA)_{1-x}(en)_x(Pb)_{1-0.7x}(I)_{3-0.4x}$ ,<sup>24</sup>  
4  
5 there is no significant shift of diffraction lines in the XRD patterns of  $T_{0.04}$  and  $T_{0.13}$  thin  
6  
7 films compared to the one of  $\alpha$ -FAPb phase. However, the specific features observed in the  
8  
9 XRD pattern of  $T_{0.04}$  powder compared to the one of  $\alpha$ -FAPb, which have a higher  
10  
11 I(100)/I(200) ratio ((100) line at  $13.9^\circ$ , (200) line at  $28.0^\circ$ ) and a lower I(210) intensity  
12  
13 ((210) line at  $31.4^\circ$ ), are also observed for  $T_{0.04}$  and  $T_{0.13}$  thin films (Figure S20).

14  
15  
16 The UV-visible absorption spectra of  $\alpha$ -FAPb and  $H_{0.13}$ ,  $H_{0.15}$ ,  $T_{0.04}$ ,  $T_{0.13}$  thin films are  
17  
18 compared in Figure 3b, and the optical bandgaps were determined from Tauc plot graphs  
19  
20 (S.I., Figure S21) leading to 1.50 eV for  $\alpha$ -FAPb, 1.51 eV for  $T_{0.04}$ , 1.53 eV for  $H_{0.13}$  and  
21  
22  $T_{0.13}$ , 1.90 eV for  $H_{0.15}$ . For  $x \leq 0.13$ , both the observed blue shift of the bandgap and the  
23  
24 decreasing absorption intensity in the 600-800 nm range are proportional to the  $x$  value of  
25  
26 the perovskite frameworks  $[Pb_{1-x}I_{3-x}]$ , consistently with earlier findings on *d*-MAPb and  
27  
28 *hollow* perovskites.<sup>22,24</sup> Interestingly, from  $x = 0.13$  to  $x = 0.15$ , the blue shift of the optical  
29  
30 bandgap becomes huge. A similar distinctive behaviour is observed using XPS  
31  
32 measurements (Figure 3c): the valence band (VB) energies relative to the Fermi energy  
33  
34 ( $E_F - E_{VB}$ ) is found almost unchanged for  $T_{0.04}$ ,  $T_{0.13}$  and  $H_{0.13}$ , (0.59 eV, 0.63 eV and 0.64  
35  
36 eV, respectively), whereas it largely increases for  $H_{0.15}$  (1.50 eV). Meanwhile, by using  
37  
38 low-lying electronic levels of iodine (4d) or lead (4f) as a reference, it is shown that the  
39  
40 position of the VB is independent of the composition (S.I., Table S10). Besides, the XPS  
41  
42 revealed also two different types of N atom for our *d*- $\alpha$ -FAPb compounds:  $NH_3^+$  group  
43  
44 belonging to  $HEA^+/TEA^+$  and  $NH_2^+$  to  $FA^+$ . Note that, as expected, only the N atom of  
45  
46  $NH_2^+$  was observed for  $\alpha$ -FAPb (as for examples  $T_{0.13}$  and  $\alpha$ -FAPb, Figure S23). Moreover,  
47  
48 as reported with *d*-MAPb,<sup>22</sup> the incorporation of  $HEA^+/TEA^+$  cations has the consequence

1  
2  
3 to eliminate the formation of Pb(0) under continuous X-ray irradiation compared to the  
4 reference  $\alpha$ -FAPI (Figure S24).  
5

6  
7 Furthermore insight into the electronic structure of *d*- $\alpha$ -FAPI compounds has been obtained  
8 by computational investigations based on density functional theory (DFT) including spin-  
9 orbit coupling. The starting point for the calculations is the X-ray resolved structure of *d*-  
10  $\alpha$ -FAPI-**H**<sub>0.104</sub> crystal in the P4/m group with partial occupation of (0, 0, 0) and (0, 0, 0.5)  
11 lead and iodide sites (see above). As a result of the dynamical motion of the organic cation  
12 evidenced by solid state NMR spectroscopy (see above), no structural information is  
13 available for those cations. Thus, in order to compensate the negative charge of the  
14 inorganic part, Cs<sup>+</sup> cations have been placed at the center of the vacancies, where FA<sup>+</sup> are  
15 expected to be located (Figures **4a** & **4b**, and zoomed view Figure S25). As such, the  
16 distinctive nature between the three sites defined in Figure **2c** relies solely on the inorganic  
17 framework. Such a substitution has proved very useful for 3D and layered perovskites,<sup>30,31</sup>  
18 and holds whenever the molecular frontier orbitals are far above and far below the  
19 conduction (CB) and valence bands, respectively. The first structural model corresponds  
20 to an ideal 3D network with no deficiency of lead and iodide ( $x = 0.00$ ). As expected, it  
21 shows a direct bandgap at A with a computed bandgap energy  $E_G = 0.28$  eV (Figure **4a**). It  
22 is well-known that Kohn-Sham DFT dramatically underestimates bandgaps in  
23 semiconductors, although it correctly describes trends. The second structural model  
24 considers the other extreme of the experimentally determined crystal structure where all  
25 the partially occupied sites are taken empty ( $x = 0.20$ ). To retain charge neutrality,  
26 additional Cs<sup>+</sup> cations are placed at the position of missing Pb atoms, where HEA<sup>+</sup> or TEA<sup>+</sup>  
27 cations are expected to be inserted. As a result, channels appear with deficiency of lead and  
28  
29  
30  
31  
32  
33  
34  
35  
36  
37  
38  
39  
40  
41  
42  
43  
44  
45  
46  
47  
48  
49  
50  
51  
52  
53  
54  
55

1  
2  
3 iodide. Despite the extent of the transformation, the resulting band structure (Figure **4b**)  
4  
5 shows remarkably similar features to the pristine system, including a direct bandgap at A.  
6  
7 Meanwhile, the deficiency in lead and iodide atoms leads to two notable differences.  
8  
9 Firstly, the bandgap  $E_G$  undergoes a sizeable increase to 0.92 eV, which is in qualitative  
10  
11 good agreement with UV-visible spectra (Figure **3b**). Concomitantly, the bandwidth of  
12  
13 both the valence and conduction bands decreases, which is indicative of increased effective  
14  
15 masses with variations of about +50% and +40% for holes and electrons, respectively.  
16  
17 Naturally, the larger effective masses of charge carriers hinder the optoelectronic properties  
18  
19 of  $x = 0.20$  material by lowering the probability to extract charges in the case of solar cells.  
20  
21  
22  
23  
24  
25  
26  
27  
28  
29  
30  
31  
32  
33  
34  
35  
36  
37  
38  
39  
40  
41  
42  
43  
44  
45  
46  
47  
48  
49  
50  
51  
52  
53  
54  
55  
56  
57  
58  
59  
60

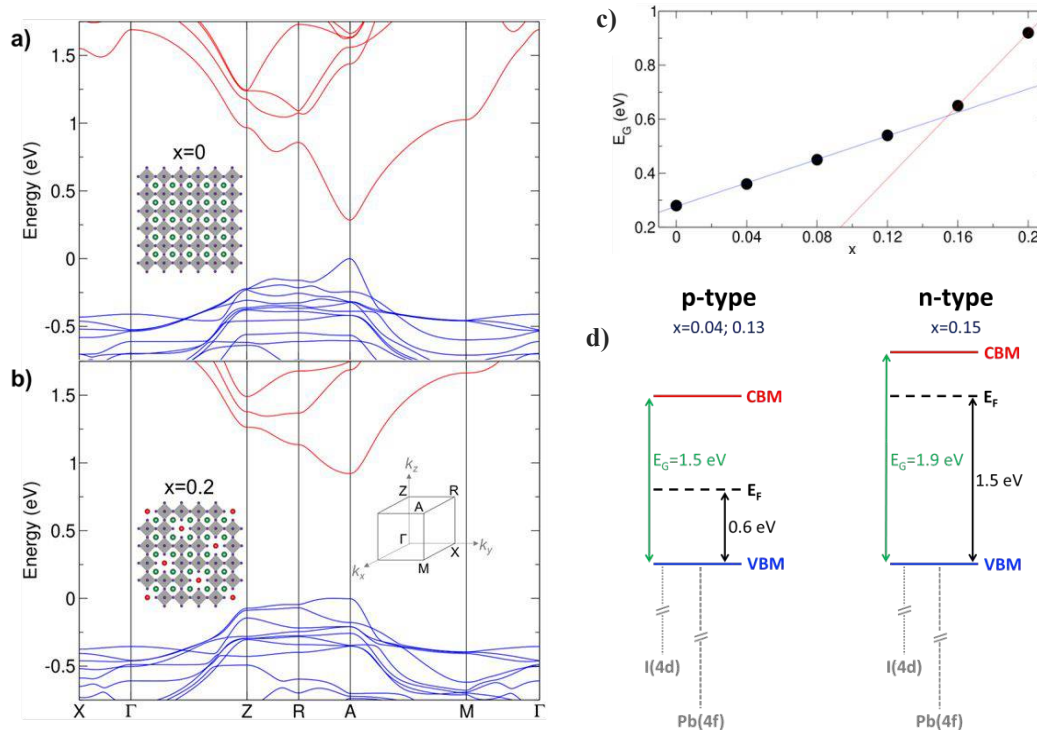


**Figure 4.** **a)** Electronic band structure for the structure deprived of lead vacancy. **b)** Same for a concentration of vacancies  $x = 0.2$ . Insets present the structure used for calculations with Pb and I atoms in grey and violet, respectively. Green and red balls show the positions of Cs<sup>+</sup> cations. Red balls mark the position of PbI vacancies. **c)** Computed bandgap  $E_G$  (eV) with respect to the vacancy concentration  $x$ . Lines in blue and red correspond to linear fits plotted as guide for the eye. **d)** Schematic evolution of band edges and Fermi level position derived from XPS and DFT results.

1  
2  
3 To further investigate the impact of composition, we designed a supercell (see S.I., Figure  
4 S25). This supercell allows to consider structural defective compositions with  $x = 0.00$ ,  
5  
6  
7  
8  
9  
10  
11  
12  
13  
14  
15  
16  
17  
18  
19  
20  
21  
22  
23  
24  
25  
26  
27  
28  
29  
30  
31  
32  
33  
34  
35  
36  
37  
38  
39  
40  
41  
42  
43  
44  
45  
46  
47  
48  
49  
50  
51  
52  
53  
54  
55  
56  
57  
58  
59  
60

To further investigate the impact of composition, we designed a supercell (see S.I., Figure S25). This supercell allows to consider structural defective compositions with  $x = 0.00$ , 0.04, 0.08, 0.12, 0.16 and 0.20 and monitor the evolution of  $E_G$  with respect to  $x$  (Figure 4c). As expected, a monotonous increase of  $E_G$  is obtained between the two end compositions but, two regions can be identified marked by a steep opening of the bandgap for  $x > 0.12$  much greater than the one observed for  $x \leq 0.12$ . (blue and red lines on Figure 4c). Indeed, the linear opening of the bandgap seen for  $x > 0.12$  is three times steeper than the one observed for  $x \leq 0.12$ . This computationally acceleration of bandgap opening for  $x > 0.12$  are qualitatively in line with the large variation of  $E_G$  and  $E_F - E_{VB}$  experimentally observed by UV-visible spectrometry and XPS, respectively, when increasing  $x$  from 0.13 to 0.15 (Figure 3b and 3c). In addition, considering the Pb 5d orbitals of as a reference, DFT calculations also confirm that the valence band energy is hardly affected in this range of composition, as the systematic downshift with increasing  $x$  value remains below 100meV.

Thus, despite the limitations of the here-presented computational model, in which the  $x$  value is monitored by considering an increasing number of infinite channels of defects starting from the experimental structure recorded on the single crystal  $(\text{HEA})_{0.406}(\text{FA})_{0.698}[\text{Pb}_{0.896}\text{I}_{2.896}] (\mathbf{H}_{0.104})$ , DFT results recover qualitatively both experimental trends obtained on thin films. These experimental and computed results suggest different band diagrams for  $x \leq 0.13$  and  $x > 0.13$  that are schematically sketched in Figure 4d. It shows that the Fermi level is closer to the VB for the less-deficient ( $x \leq 0.13$ ) compositions, which is characteristic of a p-type semiconductor with positive charges as the majority charge carriers. On the contrary, for  $x = 0.15$ , the Fermi level is found closer

1  
2  
3 to the conduction band edge, indicative of a n-type semiconductor. Recently, G. Paul *et al.*  
4  
5 inferred a correlation between electronic conductivity from p-type to n-type with PbI<sub>2</sub>-  
6  
7 deficient and PbI<sub>2</sub> rich precursors both for MAPI and FAPI.<sup>32</sup> Unfortunately, for the *d*-  
8  
9 FAPI investigated in our work, any attempt to correlate composition to stoichiometry of  
10  
11 precursors failed and the overall trend is found in the opposite direction as the films with  $x$   
12  
13 = 0.15 have been made using a stoichiometric ratio more PbI<sub>2</sub>-deficient than the one used  
14  
15 for  $x \leq 0.13$  (Table S10). This suggests that other factors can influence the semiconductor  
16  
17 doping type and level. Amongst others, it has been shown that thermal annealing can  
18  
19 convert an initially p-type halide perovskite to n-type.<sup>33</sup>  
20  
21  
22  
23  
24  
25  
26  
27  
28  
29  
30  
31  
32  
33  
34  
35  
36  
37  
38  
39  
40  
41  
42  
43  
44  
45  
46  
47  
48  
49  
50  
51  
52  
53  
54  
55  
56  
57  
58  
59  
60

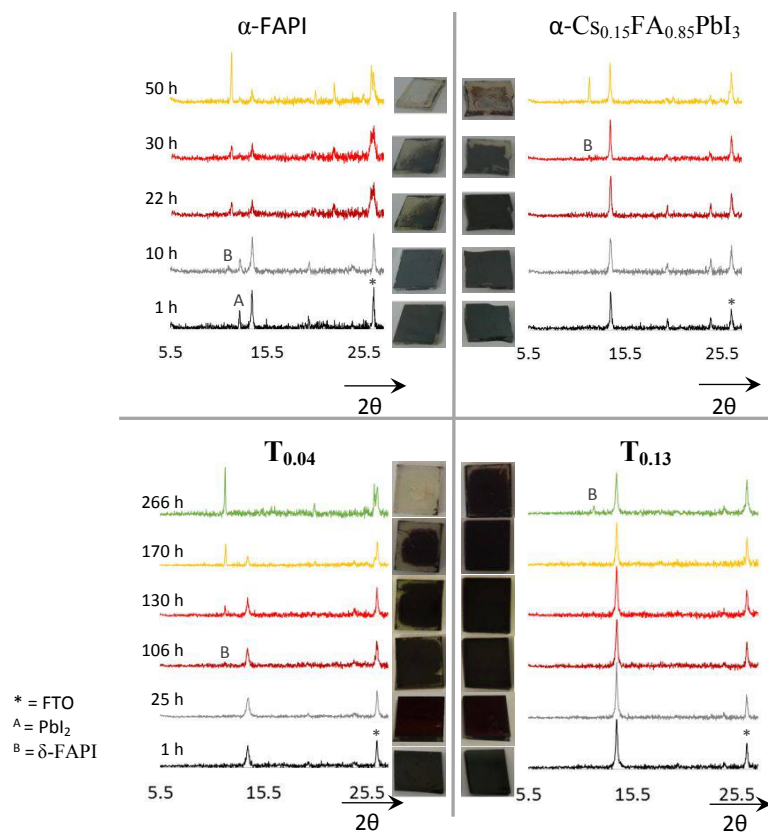


**Figure 5.** Stability test (ambient conditions: 25 °C, 75-90% humidity) of  $\alpha$ -FAPbI<sub>3</sub>,  $\alpha$ -Cs<sub>0.15</sub>FA<sub>0.85</sub>PbI<sub>3</sub>, **T**<sub>0.04</sub>, **T**<sub>0.13</sub> thin films. The XRD patterns and the pictures were realized in the 1-50 hours range and 1-266 hours range for  $\alpha$ -FAPbI<sub>3</sub>,  $\alpha$ -Cs<sub>0.15</sub>FA<sub>0.85</sub>PbI<sub>3</sub> and **T**<sub>0.04</sub>, **T**<sub>0.13</sub>, respectively.

The  $\alpha$ -phase air stability of **H**<sub>0.13</sub>, **H**<sub>0.15</sub>, **T**<sub>0.04</sub> and **T**<sub>0.13</sub> thin films has been compared to both  $\alpha$ -FAPbI<sub>3</sub> and  $\alpha$ -Cs<sub>0.15</sub>FA<sub>0.85</sub>PbI<sub>3</sub> samples. This mixed cation  $\alpha$ -FAPbI<sub>3</sub> type perovskite has been selected as a reference material due to its higher  $\alpha$ -phase stability and performances in solar cells.<sup>11,34,35</sup> The corresponding thin films were prepared by spin-coating with a final annealing step at 125 °C for  $\alpha$ -Cs<sub>0.15</sub>FA<sub>0.85</sub>PbI<sub>3</sub>, **H**<sub>0.13</sub>, **H**<sub>0.15</sub>, **T**<sub>0.04</sub>, **T**<sub>0.13</sub>, and at 155°C for  $\alpha$ -FAPbI<sub>3</sub> (more details in S.I. -X-). All these films were aged under ambient conditions (25



1  
2  
3 °C, air with 75-90% humidity, ambient sunlight), without encapsulation and their aspect  
4 and structural changes upon aging were followed (Figure 5 and Figures S26, S27). After 1  
5  
6 hour, only the XRD pattern of  $\alpha$ -FAPbI<sub>3</sub> thin film presented the typical peak of PbI<sub>2</sub> (12.8°  
7  
8 2 $\theta$ ), a compound which is in fact generated during the annealing step at 155°C. After 10  
9  
10 hours, the typical line of  $\delta$ -FAPbI<sub>3</sub> at 11.7° 2 $\theta$  appeared in the XRD pattern of  $\alpha$ -FAPbI<sub>3</sub>, then  
11  
12 the  $\alpha$ -to- $\delta$  phase transformation was completed after around 50 hours of aging.  $\alpha$ -  
13  
14 Cs<sub>0.15</sub>FA<sub>0.85</sub>PbI<sub>3</sub> thin film owns a higher  $\alpha$ -phase stability under ambient conditions than  $\alpha$ -  
15  
16 FAPbI<sub>3</sub> since the  $\alpha$ -to- $\delta$  transformation starts after 30 hours and is completed between 50 and  
17  
18 106 hours of aging (S.I. Figure S27). The **H**<sub>0.13</sub> and **H**<sub>0.15</sub> thin films exhibited a similar  
19  
20 stability to the  $\alpha$ -FAPbI<sub>3</sub> one (total transformation into  $\delta$ -FAPbI<sub>3</sub> between 22 and 50 hours of  
21  
22 aging, Figure S26). Importantly, the **T**<sub>0.04</sub> and **T**<sub>0.13</sub> thin films were significantly more  
23  
24 stable. Indeed, the first sign of  $\delta$ -phase formation occurred after 106 hours and 266 hours  
25  
26 for **T**<sub>0.04</sub> and **T**<sub>0.13</sub>, respectively. This means that under ambient conditions, **T**<sub>0.13</sub> thin films  
27  
28 are approximately twenty times more stable than  $\alpha$ -FAPbI<sub>3</sub> and ten times more stable than  $\alpha$ -  
29  
30 Cs<sub>0.15</sub>FA<sub>0.85</sub>PbI<sub>3</sub>. This exceptional  $\alpha$ -phase stability is presumably the consequence of the  
31  
32 presence of the TEA<sup>+</sup> cation inside the 3D perovskite network. Interestingly, taking into  
33  
34 account that HEA<sup>+</sup> and TEA<sup>+</sup> cations own the same alkyl chain, and that their size and  
35  
36 amounts of incorporation are similar, such a higher stability of **T**<sub>0.13</sub> compared to **H**<sub>0.13</sub>, is  
37  
38 due to added benefit thanks to the thiol function as compared to the alcohol one. The thiol  
39  
40 function is less hydrophilic and may make stronger interactions with the inorganic network,  
41  
42 thus allowing a better stabilisation of the  $\alpha$ -phase in air condition. This hypothesis of  
43  
44 stronger interactions with the inorganic network is reinforced by the solid NMR data,  
45  
46  
47  
48  
49  
50  
51  
52  
53  
54  
55  
56  
57  
58  
59  
60

1  
2  
3 which evidenced that TEA<sup>+</sup> presents much less rotational mobility as compared to the two  
4  
5 other organic cations considered in this work (FA<sup>+</sup>, HEA<sup>+</sup>).  
6  
7

## 8 9 10 **CONCLUSION**

11  
12 In summary, we have shown that both HEA<sup>+</sup> and TEA<sup>+</sup> large cations (effective radius of  
13  
14 3.44 Å and 4.14 Å, respectively) can be incorporated into a 3D [Pb<sub>1-x</sub>I<sub>3-x</sub>] α-FAPI type  
15  
16 perovskite network, showing that it is possible to circumvent the geometrical Goldschmidt  
17  
18 factor. The resulting phases *d*-α-FAPI-**H**<sub>x</sub> and *d*-α-FAPI-**T**<sub>x</sub> can be obtained by an easy  
19  
20 precipitation method at room temperature, while the well-known α-FAPI parent phase can  
21  
22 only be obtained above 150 °C. Incorporation of such larger size cations, particularly the  
23  
24 thiol-cation TEA<sup>+</sup>, leads to thin films demonstrating exceptional α-phase stability under  
25  
26 ambient conditions, surpassing the one of α-FAPI and α-Cs<sub>0.15</sub>FA<sub>0.85</sub>PbI<sub>3</sub> by more than an  
27  
28 order of magnitude. The higher α-phase stability of *d*-α-FAPI-**T**<sub>x</sub> materials compared to *d*-  
29  
30 α-FAPI-**H**<sub>x</sub> ones, points out the positive impact of the thiol function compared to alcohol  
31  
32 function. This certainly originates from the less hydrophilic nature of –SH compared to –  
33  
34 OH, and it may also indicate greater abilities of the thiol function to make quite strong  
35  
36 interactions with the inorganic perovskite network, which leads to a slower motion of the  
37  
38 TEA<sup>+</sup> cations as evidenced by solid-state NMR. Besides, computational investigations  
39  
40 correlated with experimental observations reveal the progressive opening of the direct band  
41  
42 gap and increase of the effective masses when *x* increase from 0 to 0.13. For greater values  
43  
44 of *x*, those trends remain but the evolution dramatically accelerates. Moreover, UV-visible,  
45  
46 XPS and computational results suggest that *d*-α-FAPI compounds turn from p-type to n-  
47  
48 type semiconductors for *x* values above 0.15. These observations prove that it is possible  
49  
50  
51  
52  
53  
54  
55

1  
2  
3 to accurately tune the electronic properties of this  $d$ - $\alpha$ -FAPbI<sub>3</sub> phases lead and iodide  
4 deficient hybrid perovskite family ( $d$ -HP) by controlling  $x$ . Thus,  $d$ - $\alpha$ -FAPbI<sub>3</sub> materials  
5 appears as serious MA<sup>+</sup> and Br<sup>-</sup>-free candidates as an alternative to the widespread alloys  
6 (Cs,MA,FA)Pb(I,Br)<sub>3</sub> for single junction but also tandem PSCs, which recently achieved  
7 certified power conversion efficiencies of 28.0%.<sup>3</sup> We believed that these results pave a  
8 path to the discovery of new perovskite materials for energy applications thanks to the  
9 greater versatility of defective sites.  
10  
11  
12  
13  
14  
15  
16  
17  
18  
19  
20

## 21 **ASSOCIATED CONTENT**

22 Supporting Information

23 The Supporting Information is available free of charge on the

24 ACS Publications website  
25  
26  
27  
28  
29  
30  
31  
32

## 33 **AUTHOR INFORMATION**

34 Corresponding Authors

35 [nicolas.mercier@univ-angers.fr](mailto:nicolas.mercier@univ-angers.fr) ; [claudine.katan@univ-rennes1.fr](mailto:claudine.katan@univ-rennes1.fr)  
36  
37  
38  
39

## 40 **ACKNOWLEDGEMENTS**

41 We thank Romain Mallet and the SCIAM service for the EDX-MEB measurements,  
42 Valérie Bonin and Cécile Mézière for the elemental analyses of CHNS and O, and the  
43 company Crealins for the accurate microanalysis of lead. M.K. and C.K. acknowledge  
44 support from Agence Nationale pour la Recherche (TRANSHYPERO project).  
45 Computational investigations were conducted thanks to HPC resources provided by  
46 [TGCC/CINES/IDRIS] under the allocation 2018-A0010907682 made by GENCI.  
47  
48  
49  
50  
51  
52  
53  
54  
55

**REFERENCES**

- (1) Brenner, T. M.; Egger, D. A.; Kronik, L.; Hodes, G.; Cahen, D. Hybrid Organic-Inorganic Perovskites: Low-Cost Semiconductors with Intriguing Charge-Transport Properties. *Nature Reviews Materials*. **2016**, *1*, 15007.
- (2) Song, Z.; McElvany, C. L.; Phillips, A. B.; Celik, I.; Krantz, P. W.; Wathage, S. C.; Liyanage, G. K.; Apul, D.; Heben, M. J. A Technoeconomic Analysis of Perovskite Solar Module Manufacturing with Low-Cost Materials and Techniques. *Energy Environ. Sci.* **2017**, *10*, 1297-1305.
- (3) National Renewable Energy Laboratory, N.R.E.L. Accessed 17 December 2018. <https://www.nrel.gov/pv/assets/pdfs/pv-efficiency-chart.20181214.pdf>.
- (4) Lee, M. M.; Teuscher, J.; Miyasaka, T.; Murakami, T. N.; Snaith, H. J. Efficient Hybrid Solar Cells Based on Meso-Superstructured Organometal Halide Perovskites. *Science*. **2012**, *338*, 643-647.
- (5) Kadro, J. M.; Pellet, N.; Giordano, F.; Ulianov, A.; Müntener, O.; Maier, J.; Grätzel, M.; Hagfeldt, A. Proof-of-Concept for Facile Perovskite Solar Cell Recycling. *Energy Environ. Sci.* **2016**, *9*, 3172-3179.
- (6) Kim, B. J.; Kim, D. H.; Kwon, S. L.; Park, S. Y.; Li, Z.; Zhu, K.; Jung, H. S. Selective Dissolution of Halide Perovskites as a Step Towards Recycling Solar Cells. *Nature Communications*. **2016**, *7*, 11735.
- (7) Aristidou, N.; Eames, C.; Islam, M. S.; Haque, S. A. Insights into the Increased Degradation Rate of CH<sub>3</sub>NH<sub>3</sub>PbI<sub>3</sub> Solar Cells in Combined Water and O<sub>2</sub> Environments. *J.Mater.Chem.A*. **2017**, *5*, 25469-25475.

1  
2  
3 (8) Correa-Baena, J.-P.; Saliba, M.; Buonassisi, T.; Grätzel, M.; Abate, A.; Tress, W.;  
4 Hagfeldt, A. Promises and Challenges of Perovskite Solar Cells. *Science*. **2017**, *358*, 739-  
5 744.

6  
7  
8  
9  
10 (9) Yang, W. S.; Noh, J. H.; Jeon, N. J.; Kim, Y. C.; Ryu, S.; Seo, J.; Seok, S. I. High-  
11 Performance Photovoltaic Perovskite Layers Fabricated through Intramolecular Exchange.  
12 *Science*. **2015**, *348* (6240), 1234-1237.

13  
14  
15  
16 (10) Prathapani, S.; Choudhary, D.; Mallick, S.; Bhargava, P.; Yella, A. Experimental  
17 Evaluation of Room Temperature Crystallization and Phase Evolution of Hybrid  
18 Perovskite Materials. *CrystEngComm*. **2017**, *19*, 3834-3843.

19  
20  
21  
22 (11) Li, Z.; Yang, M.; Park, J.-S.; Wei, S.-H.; Berry, J. J.; Zhu, K. Stabilizing Perovskite  
23 Structures by Tuning Tolerance Factor: Formation of Formamidinium and Cesium Lead  
24 Iodide Solid-State Alloys. *Chem. Mater*. **2016**, *28*, 284-292.

25  
26  
27  
28 (12) Pellet, N.; Gao, P.; Gregori, G.; Yang, T.-Y.; Nazeeruddin, M. K.; Maier, J.; Gratzel,  
29 M. Mixed-Organic-Cation Perovskite Photovoltaics for Enhanced Solar-Light Harvesting.  
30 *Angew. Chem. Int. Ed*. **2014**, *53*, 3151-3157.

31  
32  
33 (13) Abdi-Jalebi, M.; Andaji-Garmaroudi, Z.; Cacovich, S.; Stavrakas, C.; Philippe, B.;  
34 Richter, J. M.; Alsari, M.; Booker, E. P.; Hutter, E. M.; Pearson, A. J.; Lilliu, S.; Savenije,  
35 T. J.; Rensmo, H.; Divitini, G.; Ducati, C.; Friend, R. H.; Stranks, S. D. Maximizing and  
36 Stabilizing Luminescence From Halide Perovskites with Potassium Passivation. *Nature*.  
37 **2018**, *555*, 497-501.

38  
39  
40 (14) Cao, J.; Wu, B.; Chen, R.; Wu, Y.; Hui, Y.; Mao, B.-W.; Zheng, N. Efficient,  
41 Hysteresis-Free, and Stable Perovskite Solar Cells with ZnO as Electron-Transport Layer:  
42 Effect of Surface Passivation. *Adv. Mater*. **2018**, *30*, 1705596.

1  
2  
3 (15) Cho, K. T.; Grancini, G.; Lee, Y.; Oveisi, E.; Ryu, J.; Almora, O.; Tschumi, M.;  
4 Schouwink, P. A.; Seo, G.; Heo, S.; Park, J.; Jang, J.; Paek, S.; Garcia-Belmonte, G.;  
5 Nazeeruddin, M. K. Selective Growth of Layered Perovskites for Stable and Efficient  
6 Photovoltaics. *Energy Environ. Sci.* **2018**, *11*, 952-959.  
7  
8  
9

10  
11 (16) Zhao, Y.; Tan, H.; Yuan, H.; Yang, Z.; Fan, J. Z.; Kim, J.; Voznyy, O.; Gong, X.;  
12 Quan, L. N.; Tan, C. S.; Hofkens, J.; Yu, D.; Zhao, Q.; Sargent, E. H. Perovskite Seeding  
13 Growth of Formamidinium-Lead-Iodide-based Perovskites for Efficient and Stable Solar  
14 Cells. *Nature Communication.* **2018**, *9*, 1607.  
15  
16  
17  
18

19 (17) Gratzel, M. The Rise of Highly Efficient and Stable Perovskite Solar Cells. *Acc. Chem.*  
20 *Res.* **2017**, *50*, 487-491.  
21  
22  
23

24 (18) Saliba, M.; Matsui, T.; Domanski, K. ; Seo, J.-Y. ; Ummadisingu, A. ; Zakeeruddin,  
25 S. M.; Correa-Baena, J.-P.; Tress, W. R.; Abate, A.; Hagfeldt, A.; Grätzel, M. Incorporation  
26 of Rubidium Cations into Perovskite Solar Cells Improves Photovoltaic Performance.  
27 *Science.* **2016**, *354* (6309), 206-209.  
28  
29  
30  
31  
32

33 (19) Saliba, M.; Matsui, T.; Seo, J.-Y. ; Domanski, K. ; Correa-Baena, J.-P.; Nazeeruddin,  
34 M. K.; Zakeeruddin, S. M.; Tress, W.; Abate, A.; Hagfeldt, A.; Gratzel, M. Cesium-  
35 Containing Triple Cation Perovskite Solar Cells: Improved Stability, Reproducibility and  
36 High Efficiency. *Energy Environ. Sci.* **2016**, *9*, 1989-1997.  
37  
38  
39  
40  
41  
42

43 (20) Wang, P.; Ulfa, M.; Pauporté, T. Effects of Perovskite Monovalent Cation  
44 Composition on the High and Low Frequency Impedance Response of Efficient Solar  
45 Cells. *J. Phys. Chem. C.* **2018**, *122*, 1973-1981.  
46  
47  
48  
49  
50  
51  
52  
53  
54  
55

1  
2  
3 (21) Turren-Cruz, S.-H.; Hagfeldt, A.; Saliba, M. Methylammonium-Free, High-  
4 Performance and Stable Perovskite Solar Cells on a Planar Architecture. *Science*. **2018**,  
5  
6 362 (6413), 449-453.  
7

8  
9  
10 (22) (a) Leblanc, A.; Mercier, N. ; Allain, M. ; Dittmer, J. ; Fernandez, V. ; Pauporté, T.  
11  
12 Lead- and Iodide-Deficient (CH<sub>3</sub>NH<sub>3</sub>)PbI<sub>3</sub> (*d*-MAPI): The Bridge between 2D and 3D  
13  
14 Hybrid Perovskites. *Angew. Chem.* **2017**, 129, 16283-16288. (b) Patent CRO BFF  
15  
16 17P0180, Project (1), 14<sup>th</sup> March **2017**, Depositor SATT OUEST VALORISATION –  
17  
18 Client reference: DV3293.  
19

20  
21 (23) Tsai, C.-M.; Lin, Y.-P. ; Pola, M. K. ; Narra, S. ; Jokar, E. ; Yang, Y.-W. ; Diao, E.  
22  
23 W.-G. Control of Crystal Structures and Optical Properties with Hybrid Formamidinium  
24  
25 and 2-Hydroxyethylammonium Cations for Mesoscopic Carbon-Electrode Tin-Based  
26  
27 Perovskite Solar Cells. *ACS Energy Lett.* **2018**, 3, 2077-2085.  
28  
29

30  
31 (24) Spanopoulos, I.; Ke, W.; Stoumpos, C. C.; Schueller, E. C. ; Kontsevoi, O. Y. ;  
32  
33 Seshadri, R. ; Kanatzidis, M. G. Unraveling the Chemical Nature of the 3D “Hollow”  
34  
35 Hybrid Halide Perovskites. *J. Am. Chem. Soc.* **2018**, 140, 17, 5728-5742.  
36  
37

38 (25) Kieslich, G.; Sun, S.; Cheetham, A. K. Solid-State Principles Applied to Organic-  
39  
40 Inorganic Perovskites: New Tricks for an Old Dog. *Chem. Sci.* **2014**, 5, 4712-4715.  
41

42 (26) Weller, M. T.; Weber, O. J.; Frost, J. M.; Walsh, A. Cubic Perovskite Structure of  
43  
44 Black Formamidinium Lead Iodide,  $\alpha$ -[HC(NH<sub>2</sub>)<sub>2</sub>]PbI<sub>3</sub>, at 298 K. *J. Phys. Chem. Lett.*  
45  
46 **2015**, 6, 3209-3212.  
47

48  
49 (27) Taylor, V. C. A.; Tiwari, D.; Duchi, M.; Donaldson, P. M.; Clark, I. P.; Fermin, D. J.;  
50  
51 Oliver, T. A. A. Investigating the Role of the Organic Cation in Formamidinium Lead  
52  
53 Iodide Perovskite Using Ultrafast Spectroscopy. *J. Phys. Chem. Lett.* **2018**, 9, 895-901.  
54  
55

- 1  
2  
3 (28) Eperon, G. E.; Stranks, S. D.; Menelaou, C.; Johnston, M. B.; Herz, L. M.; Snaith, H.  
4 J. Formamidinium Lead Trihalide: a Broadly Tunable Perovskite for Efficient Planar  
5 Heterojunction Solar Cells. *Energy Environ. Sci.* **2014**, *7*, 982-988.  
6  
7  
8  
9  
10 (29) Kohrt, C.; Spannenberg, A.; Werner, T. 2-Hydroxyethylammonium Iodide. *Acta*  
11 *Cryst.* **2014**, *E70*, o628. DOI : 10.1107/S1600536814009581.  
12  
13  
14 (30) Even, J.; Pedesseau, L.; Katan, C. Proc. SPIE, 2014, 9140, 91400Y.  
15  
16 (31) Even, J.; Pedesseau, L.; Jancu, J.-M.; Katan, C. Importance of Spin-Orbit Coupling in  
17 Hybrid Organic/Inorganic Perovskites for Photovoltaic Applications. *J. Phys. Chem. Lett.*  
18 **2013**, *4*, 2999-3005.  
19  
20  
21  
22 (32) Paul, G.; Chatterjee, S.; Bhunia, H.; Pal, A. J. Self-Doping in Hybrid Halide  
23 Perovskites via Precursor Stoichiometry: To Probe the Type of Conductivity through  
24 Scanning Tunneling Spectroscopy. *J. Phys. Chem. C.* **2018**, *122*, 35, 20194-20199.  
25  
26  
27  
28 (33) Wang, Q.; Shao, Y.; Xie, H.; Lyu, L.; Liu, X.; Gao, Y.; Huang, J. Qualifying  
29 Composition Dependent p and n Self-Doping in CH<sub>3</sub>NH<sub>3</sub>PbI<sub>3</sub>. *Applied Physics Letters.*  
30 **2014**, *105*, 163508.  
31  
32  
33  
34 (34) Song, Z.; Wang, C.; Phillips, A. B.; Grice, C. R.; Zhao, D.; Yu, Y.; Chen, C.; Li, C.;  
35 Yin, X.; Ellingson, R. J.; Heben, M. J.; Yan, Y. Probing the Origins of Photodegradation  
36 in Organic-Inorganic Metal Halide Perovskites with Time-Resolved Mass Spectrometry.  
37 *Sustainable Energy Fuels.* **2018**, *2*, 2460-2467.  
38  
39  
40 (35) Lee, J.-W.; Kim, D.-H.; Kim, H.-S.; Seo, S.-W.; Cho, S. M.; Park, N.-G.  
41 Formamidinium and Cesium Hybridization for Photo- and Moisture-Stable Perovskite  
42 Solar Cell. *Adv. Energy Mater.* **2015**, *5*, 1501310.  
43  
44  
45  
46  
47  
48  
49  
50  
51  
52  
53  
54  
55  
56  
57  
58  
59  
60



1  
2  
3 (36) Mercier, N.; Poiroux, S.; Riou, A.; Batail, P. Unique Hydrogen Bonding Correlating  
4 with a Reduced Band Gap and Phase Transition in the Hybrid Perovskites  
5  
6 (HO(CH<sub>2</sub>)<sub>2</sub>NH<sub>3</sub>)<sub>2</sub>PbX<sub>4</sub> (X = I, Br). *Inorganic Chemistry*. **2004**, *43*, 26, 8361-8366.  
7

8  
9  
10 (37) Soler, J. M.; Artacho, E.; Gale, J. D.; García, A.; Junquera, J.; Ordejón, P.; Sánchez-  
11 Portal, D. The SIESTA Method for ab initio Order-N Materials Simulation. *J. Phys.:*  
12 *Condens. Matter*. **2002**, *14*, 2745-2779.  
13  
14

15  
16  
17 (38) Artacho, E.; Anglada, E.; Diéguez, O.; Gale, J. D.; García, A.; Junquera, J.; Martin,  
18 R. M.; Ordejón, P.; Pruneda, J. M.; Sánchez-Portal, D. ; Soler, J. M. The SIESTA Method;  
19 Developments and Applicability. *J. Phys.: Condens. Matter*. **2008**, *20*, 064208.  
20  
21

22  
23  
24 (39) Zhang, Y.; Yang, W. Generalized Gradient Approximation Made Simple. *Phys. Rev.*  
25 *Lett*. **1998**, *80*, 890.  
26  
27

28  
29 (40) Troullier, N.; Martins, J. L. Efficient Pseudopotentials for Plane-Wave Calculations.  
30 *Phys. Rev. B*. **1991**, *43*, 1993-2006.  
31  
32

33  
34 (41) Artacho, E.; Sánchez-Portal, D.; Ordejón, P.; García, A.; Soler, J. M. Linear-Scaling  
35 ab-initio Calculations for Large and Complex Systems. *Phys. Stat. Sol. (b)* **1999**, *215*, 809-  
36  
37 817.  
38

39  
40 (42) Fernández-Seivane, L.; Oliveira, M. A.; Sanvito, S.; Ferrer, J. On-Site Approximation  
41 for Spin-Orbit Coupling in Linear Combination of Atomic Orbitals Density Functional  
42  
43 Methods. *J. Phys.: Condens. Matter*. **2006**, *18*, 7999-8013.  
44  
45  
46  
47  
48  
49  
50  
51  
52  
53  
54  
55

## Table of contents

